American Mineralogist, Volume 82, pages 1241–1254, 1997

High-grade contact metamorphism of calcareous rocks from the Oslo Rift, Southern Norway

BJØRN JAMTVEIT,[1] SVEN DAHLGREN,[2] AND HAAKON AUSTRHEIM[3]

[1]Department of Geology, University of Oslo, P.O. Box 1047 Blindern, N-0316 Oslo, Norway
[2]The Norwegian Petroleum Directorate, P.O. Box 600, 4001 Stavanger, Norway
[3]Mineralogical-Geological Museum, Sars gt.1, N-0562 Oslo, Norway

ABSTRACT

Shallow-level plutons caused extensive contact metamorphism of Lower Paleozoic shale and carbonate sequences in the Permian Oslo Rift. A >500 m long and 100 m wide shale-limestone xenolith embedded within monzonites belonging to the Skrim plutonic complex experienced high-grade contact metamorphism and generation of minerals and mineral assemblages rarely reported from metamorphic rocks. The peak metamorphic (Stage I) assemblages in calcite-saturated rocks include wollastonite, melilites, fassaitic pyroxenes, phlogopite, titanian grossular, kalsilite, nepheline, perovskite, cuspidine, baghdadite, pyrrhotite, and occasional graphite. Mineral reactions involving detrital apatite produced a series of silicate apatites, including the new mineral species $Ca_{3.5}(Th,U)_{1.5}Si_3O_{12}(OH)$. This assemblage equilibrated at T = 820–870 °C with a C-rich, internally buffered pore-fluid (20–40 mol% CO_2 + CH_4). During cooling the shale-limestone xenolith experienced infiltration of C-poor (< 0.1 mol% CO_2) fluids, triggering the formation of retrograde (Stage II) mineral assemblages comprising monticellite, tilleyite, vesuvianite, grandite garnets, diopside, and occasional hillebrandite. Rare potassium iron sulfides (rasvumite and djerfisherite) formed at the expense of primary pyrrhotite. These assemblages probably formed near 700 °C. Formation of diffuse sodalite-bearing veinlets was associated with breakdown of nepheline and the replacement of kalsilite and wollastonite by potassium feldspar. The sodalite-bearing Stage III assemblage formed by the infiltration of saline brines at a maximum temperature of 550 °C. Low-temperature (Stage IV) retrogression of the Stage I-III assemblage produced scawtite, giuseppettite, hydrogrossulars, phillipsite, thomsonite, and three hitherto undescribed mineral species.

INTRODUCTION

Mineral assemblages and mineral reactions occurring during contact metamorphism of calcareous rocks have been extensively studied and described since the pioneering work by Goldschmidt (1911) in the Oslo rift. Observed mineral assemblages reflect a wide range of temperature and fluid-composition space (Tracy and Frost 1991). Equilibrium temperatures approaching and even exceeding 1000 °C are reported for limestone assemblages in aureoles around mafic intrusions (e.g., Joesten 1983). Because most mafic intrusions crystallize without releasing large quantities of volatiles, most high-grade contact metamorphic carbonate rocks have buffered the local pore-fluid composition during heating and devolatilization. High-grade assemblages reflecting equilibration with H_2O-dominated fluids are rarely reported from shallow level ($P \leq 1000$ bars) environments (see however, Williams-Jones 1981 and Inderst 1987).

In the Oslo area, contact metamorphism is related to various shallow level intrusions. Frequently devolatilization reactions in calcareous rocks are driven by infiltration of externally derived H_2O-dominated fluids (Jamtveit et al. 1992a, 1992b; Jamtveit and Andersen 1993; Svensen and Jamtveit 1998). Here, we present the first description of high-grade mineral assemblages in contact metamorphic carbonates from the Oslo rift. A large xenolith of Lower Paleozoic sedimentary rock within the Permian Skrim monzonite complex in the Southern Oslo rift experienced metamorphic temperatures exceeding the solidus of the crystallizing monzonite. Mineral reactions involving carbonate and silicate minerals led to the production of various of Si-poor silicates, including numerous phases rarely or never previously reported from metamorphic rocks. Reactions between silicates and pyrrhotite produced rare potassium iron sulfides, and reactions involving detritial apatite produced LREE and Th-rich silicate apatites including a new mineral species [$Ca_{3.5}Th_{1.5}Si_3O_{12}$ (OH)].

GEOLOGICAL SETTING

The Permo-Carboniferous Oslo paleorift is situated in the southwestern part of the Baltic shield. The exposed parts of the rift are composed of two half grabens filled with Carboniferous sedimentary rocks, alkaline volcanic

0003–004X/97/1112–1241$05.00

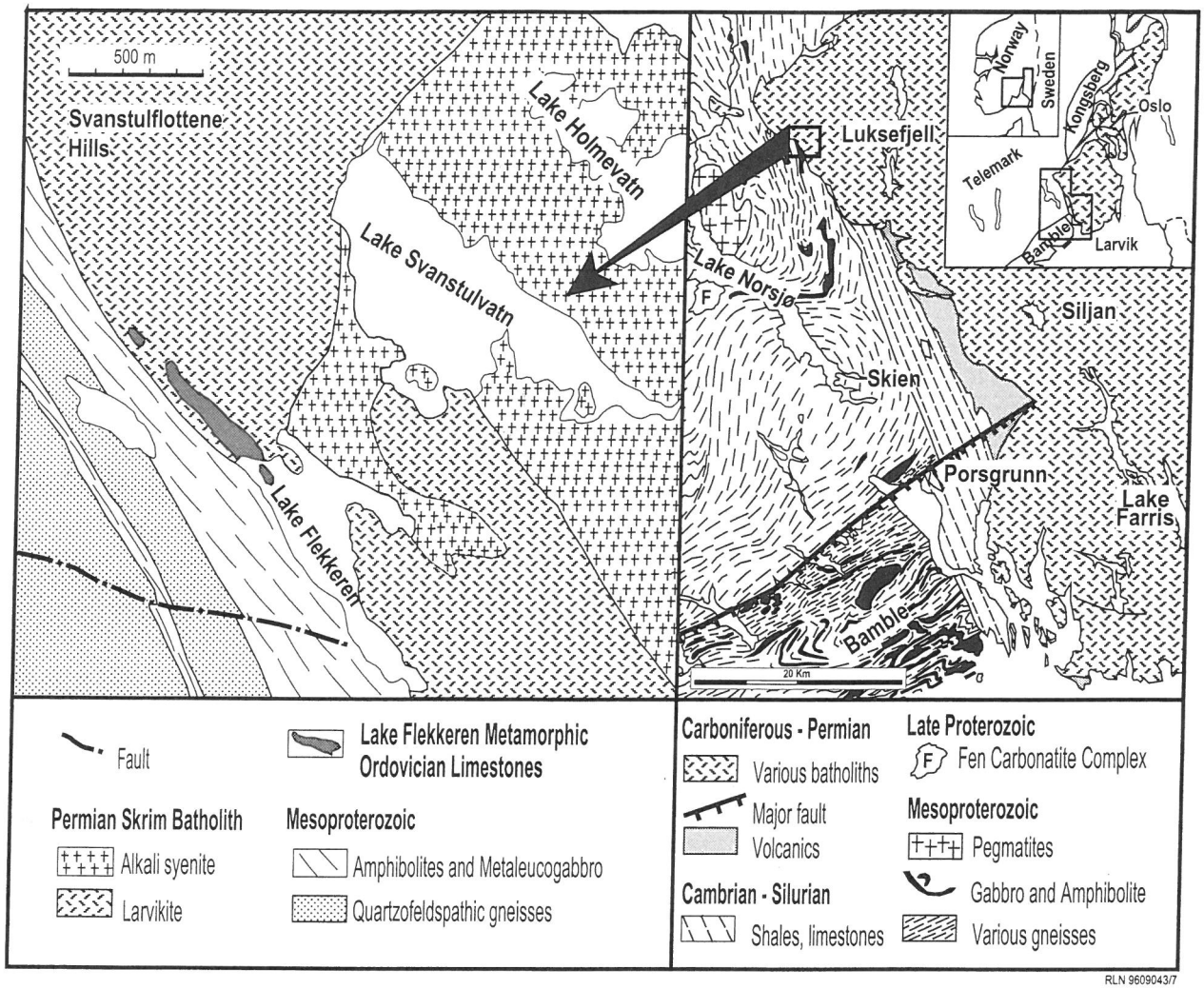

FIGURE 1. Simplified geological maps of the Flekkeren area (left; Dahlgren 1998) and the Southern margin of the Oslo rift (right; Dahlgren 1998).

and intrusive rocks, and Lower Paleozoic sedimentary rocks (Fig. 1). The latter are dominated by shales and limestones (Bjørlykke 1974). Extensive intrusive activity in the time interval 300–250 Ma (Sundvoll et al. 1990) included emplacement of various monzonitic to granitic rocks and caused widespread contact metamorphism and hydrothermal activity within the originally unmetamorphosed sedimentary rocks.

The Lower Paleozoic shales are composed of illite, chlorite, quartz, diagenetic feldspar, and occasional dolomite, whereas the limestones are dominated by calcite (Bjørlykke 1974). Both shales and limestones contain significant but generally low contents of organic carbon (< 1 wt%). During contact metamorphism, the most notable metamorphic reactions took place at the carbonate-shale contacts where metasomatic calc-silicate zones formed at the expense of the carbonate and shale layers. Maximum temperature conditions near the intrusive contacts were estimated to be in the range 400–550 °C (Jamtveit et al. 1992b; Svensen 1996), consistent with dominantly conductive heating of the aureoles.

Recent stable isotope results have demonstrated widespread pervasive infiltration of aqueous fluids with a magmatic O isotope signature around the various cooling intrusions (Jamtveit et al. 1992a, 1992b, 1997). Decarbonation reactions leading to formation of the contact metamorphic mineral assemblages are to a large extent driven by this infiltration. Reaction-enhanced porosity and permeability at the shale-carbonate contacts was a significant factor in controlling fluid release from these shallow intrusions (Jamtveit et al. 1997). The current model for fluid flow during peak contact metamorphic conditions around granitoid intrusions in the Oslo rift includes early pervasive and slow infiltration of magmatic fluids of low salinity in an overpressurized system (relative to hydrostatic), interrupted by rapid and focused release of saline solutions with associated pressure drops in high permeability zones.

TABLE 1. Abbreviations and formulas for observed minerals in limestones and calc-silicate rocks from Flekkeren

	Name	Formula	Petrografic status
ab	albite	$NaAlSi_3O_8$	Stage IV
ad	andradite	$Ca_3Fe_2Si_3O_{12}$	Stage IV
ak	akermanite	$Ca_2MgSi_2O_7$	Stage I
al	alabandite	MnS	Stage I?
an	anorthite	$CaAl_2Si_2O_8$	Stage I*
ap	apatite	$Ca_5(PO_4)_3(OH)$	detrital
au	augite (fassaite)	$Ca(Mg,Fe,Al,Ti)(Si,Al)_2O_6$	Stage I
ba	baddeleyite	ZrO_2	inclusions in zircon
bg	baghdadite	$Ca_3ZrSi_2O_9$	Stage I
br	britholite	$(LREE,Ca)_5(SiO_4,PO_4)_3(OH)$	Stage I
cc	calsite	$CaCO_3$	all assemblages
cr	chromite	$FeCr_2O_4$	detrital
cu	cuspidine	$Ca_4Si_2O_7(F,OH)_2$	Stage I
di	diopside	$CaMgSi_2O_6$	Stage II
dj	djerfisherite	$K_6(Fe,Ni)_{25}S_{26}Cl$	Stage II
ga	galena	PbS	detrital
gp	graphite	C	Stage I?
gr	grossular	$Ca_3Al_2Si_3O_{12}$	Stage II
gu	giuseppettite	$(Na,K,Ca)_{7-8}(Si,Al)_{12}O_{24}(SO_4,Cl)_{1-2}$	Stage IV
hb	hillebrandite	$Ca_2SiO_3(OH)_2$	Stage II?
hi	hibschite	$Ca_3Al_2Si_{3-x}O_{12}(OH)_{4x}$ (x = 0.2–1.5)	Stage IV
ka	katoite	$Ca_3Al_2Si_{3-x}O_{12}(OH)_{4x}$ (x = 1.5–3)	Stage IV
kfs	K-feldspar	$KAlSi_3O_8$	Stage II or III
ki	kimzeyite	$Ca_3(Zr,Ti)_2(Si,Al)_3O_{12}$	Stage I
ks	kalsilite	$KAlSiO_4$	Stage I
lö	löllingite	$FeAs_2$	detrital?
ma	marialite	$Na_4Al_3Si_9O_{24}Cl$	Stage I*
mc	marcasite	FeS_2	Stage IV
mg	magnetite	Fe_3O_4	detrital
mo	monticellite	$CaMgSiO_4$	Stage II
ne	nepheline	$NaAlSiO_4$	Stage I
op	opal	SiO_2	Stage IV
pe	perovskite	$CaTiO_3$	Stage I
ph	phlogopite	$KMg_3AlSi_3O_{10}(OH)_2$	Stage I
pi	phillipsite	$(K,Na,Ca)_{1-2}(Si,Al)_8O_{16}\cdot 6\,H_2O$	Stage IV
pt	pentlandite	$(Fe,Ni)_9S_8$	Stage I
py	pyrite	FeS_2	Stage IV
pyh	pyrrhotite	$Fe_{1-x}S$	Stage I
qz	quartz	SiO_2	Stage I*
rs	rasvumite	KFe_2S_3	Stage II
sa	saponite	$(Ca/2,Na)_{0.3}(Mg,Fe)_3(Si,Al)_4O_{10}(OH)_2\cdot 4\,H_2O$	Stage IV
sc	scawtite	$Ca_7Si_6(CO_3)O_{18}\cdot 2\,H_2O$	Stage IV
sd	sodalite	$Na_8Al_6Si_6O_{24}Cl_2$	Stage III
sh	scheelite	$CaWO_4$	detrital
so	schorlomite	$Ca_3Ti_2(Fe,Si)_3O_{12}$	Stage I
sph	sphalerite	ZnS	detrital
ta	thaumasite?	$Ca_6Si_2(CO_3)_2(SO_4)_2(OH)_{12}\cdot 24\,H_2O$	Stage IV
tb	tobermorite	$Ca_5Si_{12}O_{30}(OH)_6\cdot 4\,H_2O$	Stage IV
th	thorite	$ThSiO_4$	detrital
ti	titanite	$CaTiSiO_5$	Stage I*
tm	thomsonite	$NaCa_2Al_5Si_5O_{20}\cdot 6\,H_2O$	Stage IV
to	thorianite	ThO_2	Stage IV
ty	tilleyite	$Ca_5Si_2O_7(CO_3)_2$	Stage II
ur	uraninite	UO_2	detrital
uv	uvarovite	$Ca_3Cr_2Si_3O_{12}$	Stage I
vs	vesuvianite	$Ca_{10}Mg_2Al_4(SiO_4)_5(Si_2O_7)_2(OH)_4$	Stage II
wo	wollastonite	$CaSiO_3$	Stage I–III
zrn	zircon	$ZrSiO_4$	Stage I*
X1	new species	$Ca_{3.5}(Th,U)_{1.5}(SiO_4)_3(OH)$	Stage I
X2	new zeolite?	$Na_2CaAl_4Si_4O_{16}\cdot X\,H_2O$	Stage IV
X3	new species?	$Na_2Ca_4Si_6O_{15}(OH)_4$	Stage IV
X4	new species?	$Ca_{-0.8}Al_{-0.2}SiO_n(OH)_m\cdot X\,H_2O$	Stage IV
Y1	unid. species	LREE,Ca-Silicate(stillwellite ?)	Stage I??
Y2	unid. species	Ca,LREE,Th,U,Ti,Nb-oxide	detrital

* Only in peak assemblage of calcite-free rocks.

The *Flekkeren* limestone raft is located within the southwestern part of the Permian Skrim batholith (Fig. 1; Dahlgren 1998). The Skrim batholith consists largely of a series of alkaline plutons of larvikite (monzonite with ternary feldspar), syenites and granites, which transects north-trending Sveconorwegian (1200–1000 Ma) gneisses, quartzites, and amphibolites, easterly dipping Cambro-Silurian sedimentary rocks, and Upper Paleozoic basaltic volcanic rocks. The limestone raft (Fig. 1) is totally embedded in larvikite that was emplaced at 281 ± 1 Ma (Pedersen et al. 1995). Both

TABLE 2. Observed mineral assemblages in contact metamorphic limestones

	Stage I				Stage II				Stage III
Sample	FL15	79D	79A	79A	79B	79B	79D	FL17	FL32
cc	x	x	x	x	x				x
wo	x	x	x	x		x	x	x	x
Mel	x	x	x	x					
Grt	x		x	x	x	x	x	x	
Cpx	x		x						x
ph	x							x	
cu				x					
pe	x	x	x	x	x	x	x	x	
ks	x	x	x	x	x	x	x	x	x
ne	x	x	x	x	x	x	x	x	
vs					x	x			
mo					x	x	x	x	
ty					x	x			
kfs									x
sd									x
ti									x

Notes: Not including phases outside the KNaCaFeMgAlTiSiCOH system and late (post Stage III) reaction products. Abbreviations used for mineral groups, rather than end-members, start with an upper case letter as follows: Grt = garnet; Mel = melilite, Cpx = clinopyroxene; Sca = scapolite.

the limestone raft and the larvikite are transected by veins from a younger alkali syenite pluton that occurs immediately east of Flekkeren. The limestone raft is separated by a larvikite screen less than 10 m thick from Sveconorwegian metagabbros in the west. The stratigraphic position of the metasediments in the Flekkeren raft is not evident because the protolith was modified by the strong metamorphism. Most likely it consists of the Upper Ordovician (Caradoc-Ashgill) nodular limestones (the Steinvika formation) in the west, shales of the Venstøp formation in the middle, and nodular limestones (the Herøya formation) in the east. South of Lake Flekkeren the upper part of the Steinvika formation is underlain by about 350 m of Cambrian and Ordovician sediments (Dahlgren 1998). These underlying sediments are missing at Lake Flekkeren, and, because the distance between the basement and the limestone raft is less than 10 m, evidently the raft is displaced from its original position. The Flekkeren body is poorly exposed on the northern shore of the small lake Flekkeren, and as scattered small outcrops in the boggy area north of the lake. It constitutes a lens at least 500 m long and less than 100 m wide, and it is locally transected by small veins injected from the host plutons. The original composition of the initial sedimentary layers (millimeter to centimeter thick) varied from nearly pure limestone (calcite) layers to marly shales. The described sample material was collected from loose blocks from a recent road blasting and is limited to samples of marly limestones.

TABLE 3. Representative mineral analyses

	Garnet					Clinopyroxene		Melilite		Phlogopite		Kalsilite	Nepheline
Sample no.	Stage I Melanite FL17	Stage I Uvarovite FL-1	Stage I Kimzeyite FL-B	Stage II Grossular FL-C	Stage IV Katoite FL-C	Stage I Augite FL-A	Stage II Diopside FL-E	Stage I FL-A	Stage I FL-B	Stage I FL-A	Stage I FL-A	Stage I FL-A	Stage I FL21
SiO_2	31.68	35.40	19.68	39.29	21.95	46.40	52.42	42.98	34.89	39.57	38.30	38.89	41.67
TiO_2	9.44	1.32	10.01	0.11	0.04	1.63	0.56	0.00	0.00	0.47	0.58	0.00	0.00
Al_2O_3	7.09	0.60	8.13	17.98	23.60	8.14	1.70	5.50	17.91	17.19	17.39	30.96	34.48
Fe_2O_3	11.02	2.39	6.48	5.20	0.29	4.59	3.65	2.08	0.24	3.97	3.89	0.14	0.19
MnO	0.12	0.12	0.06	0.05	0.22	0.05	0.18	0.04	0.12	0.04	0.00	0.01	0.00
MgO	1.23	0.22	1.52	0.00	0.15	12.55	14.90	9.24	6.23	24.06	23.00	0.02	0.00
CaO	34.66	33.16	31.73	37.27	42.18	25.19	25.30	36.77	38.87	0.05	0.08	2.13	0.06
Na_2O						0.11	0.28	2.39	1.78	0.08	0.08	0.16	16.23
K_2O								0.16	0.12	9.90	10.16	26.81	8.12
Cr_2O_3	4.15	27.39	1.87	0.00	0.04	0.67	0.64	0.00	0.00	0.24	0.24	0.00	0.00
ZrO_2	0.57	0.00	18.41										
F_2O										0.80	0.88		
Total	99.95	100.60	97.89	99.91	88.47	99.34	99.66	99.15	100.17	96.36	94.64	99.12	100.75
N.B.O.	Ca + Mn + Mg = 3000					cations = 4000		cations = 5000		cations − Na − K = 14000		Si + Al = 2000	
Si	2.433	2.954	1.625	2.949	1.444	1.729	1.944	1.967	1.574	5.523	5.483	1.032	1.012
Ti	0.547	0.083	0.623	0.006	0.002	0.046	0.016	0.000	0.000	0.049	0.063	0.000	0.000
Al	0.643	0.060	0.792	1.592	1.837	0.358	0.074	0.297	0.952	2.827	2.934	0.968	0.988
Fe	0.639	0.150	0.403	0.294	0.015	0.143	0.113	0.080	0.009	0.463	0.465	0.003	0.004
Mn	0.008	0.008	0.005	0.003	0.012	0.002	0.006	0.002	0.004	0.004	0.000	0.000	0.000
Mg	0.141	0.027	0.188	0.000	0.014	0.697	0.824	0.630	0.419	5.004	4.908	0.001	0.000
Ca	2.859	2.973	2.812	3.000	2.986	1.006	1.005	1.804	1.879	0.008	0.012	0.061	0.001
Na						0.008	0.020	0.210	0.160	0.020	0.023	0.008	0.764
K								0.009	0.007	1.762	1.856	0.908	0.252
Cr	0.253	1.812	0.122	0.000	0.002	0.020	0.019			0.027	0.027		
Zr	0.021	0.000	0.743										
OH*	1.940	0.184		0.204	6.224								
F										0.360	0.400		

Note: N.B.O. = Normalization based on.
* OH = 4*[3000 − Si − Ti(4+)].

Petrography and mineral chemistry

The analyzed samples from Flekkeren contain more than 60 different mineral species formed at various stages during the contact metamorphic history. Petrographic and microprobe studies were carried out by the JEOL JSM-840 electron microscope at the Department of Geology and by the CAMECA CAMEBAX electron microprobe at the Mineralogical-Geological Museum, both at the University of Oslo, using natural and synthetic standards. All analyses were run at an accelerating voltage of 15 kV. Beam currents varied from 10 to 20 nA depending on the phase to be analyzed. Peak and background intensities were counted for 10 s for the most abundant elements (e.g., Si) and for 20 s for elements with lower concentrations. Mineral abbreviations, end-member compositions, and mode of occurrence are given in Table 1 and observed mineral assemblages relevant for the phase petrological analysis are listed in Table 2. Representative mineral analyses are given in Tables 3 and 4.

In the following, the observed minerals and mineral assemblages are related to four different stages (I–IV) in the contact metamorphic evolution. This does not imply that we assume that the metamorphic process has taken place as a series of events, but is an attempt to separate minerals and assemblages that seem to be related in space and time.

Stage I

Stage I represents the peak metamorphic conditions. At this stage, calcite in carbonate-rich rocks is typically coarse grained (grain size of several millimeters) and displays polygonal foam textures. Carbonate-poor rocks are more fine grained (typical grain diameter 0.01–1 mm), and the silicate minerals commonly display textures indicative of very short transport distances during growth (such as complex graphic intergrowths). Carbonate-bearing lithologies contain wollastonite, kalsilite, nepheline, melanite garnet, perovskite, cuspidine, baghdadite, pyrrhotite (Fe/S = 0.84–0.93), occasional alabandite, one or more apatite-group minerals, and occasional graphite as scattered, apparently corroded grains.

The bulk composition of the analyzed layered samples varies significantly on millimeter scale. Some domains contain the assemblage Mel+Cpx+Ph+Wo+Cc+Ks (Fig. 2a), which represents an isobaric invariant assemblage in the $KAlO_2$-CaO-MgO-SiO_2-H_2O-CO_2 system.

Clinopyroxene commonly occurs as poikiloblasts (occasionally many millimeters across) with inclusions of wollastonite, phlogopite, and kalsilite. A continuous range occurs in clinopyroxene compositions from the Stage I augites (fassaites) containing up to 10.9 wt% Al_2O_3 (0.5 Al apfu), 2.6 wt% TiO_2, and 0.75 wt% Cr_2O_3 to the nearly pure diopsides formed during retrogression (Stage II; see Table 3).

Table 3—*Extended*

	Cuspidine		Baghdadite		Vesuvianite		Monticellite	
Sample no.	Stage I FL-B	Stage I FL-B	Stage I FL-B	Stage I FL-B	Stage II FL-D	Stage II FL-D	Stage II FL17	Stage II FL-B
SiO_2	32.24	32.54	29.09	29.36	37.18	36.94	36.84	37.50
TiO_2	0.02	0.02	2.70	3.02	1.03	0.77	0.00	0.00
Al_2O_3					16.67	16.93	1.47	0.02
Fe_2O_3	0.00	0.00			1.85	1.84	9.51	1.75
MnO	0.03	0.00			0.00	0.04	0.46	0.70
MgO					3.38	3.32	16.24	22.95
CaO	60.05	59.93	41.42	42.16	36.81	36.53	35.12	36.30
Na_2O					0.03	0.03		
K_2O					0.02	0.02		
Cr_2O_3							0.01	0.00
ZrO_2	1.32	1.70	25.52	23.72				
F_2O	10.46	10.34						
Total	99.34*	99.80*	98.73	98.25	96.98	96.48	99.65	99.22
N.B.O.	cations = 6000				cations = 25 000			
Si	1.989	2.000	1.984	1.992	10.829	10.806	1.016	0.998
Ti	0.001	0.001	0.139	0.154	0.177	0.132	0.000	0.000
Al					5.054	5.156	0.048	0.001
Fe	0.000	0.000			0.271	0.271	0.219	0.039
Mn	0.001	0.000			0.000	0.006	0.011	0.016
Mg					1.139	1.121	0.667	0.911
Ca	3.969	3.947	3.028	3.066	7.515	7.489	1.038	1.035
Na					0.010	0.010		
K					0.010	0.010		
Cr							0.000	0.000
Zr	0.040	0.051	0.849	0.785				
OH*								
F	2.041	2.010						

* Total − 0 ≡ F

TABLE 4. Representative silicate-phosphate analyses

Sample no.	FL-7	FL-7	FL-7	FL-7	FL-7	FL-7	FL-7	FL-7	FL-7	FL-7	FL-7	FL-7
SiO_2	19.52	19.06	18.78	18.81	20.32	20.66	17.46	17.63	18.05	17.39	18.68	0.45
P_2O_5	1.65	3.45	1.95	4.21	1.11	0.98	6.13	5.61	6.18	6.54	4.88	40.63
CaO	23.27	24.74	23.87	24.83	20.05	19.45	26.36	25.89	25.30	25.61	21.51	56.23
Ce_2O_3	3.01	4.25	3.71	4.26	12.08	11.85	11.20	11.02	13.76	11.77	20.61	0.48
La_2O_3	2.36	3.12	2.80	3.21	8.01	7.85	7.10	7.17	8.75	7.68	12.95	0.32
Nd_2O_3	0.44	0.83	0.91	0.80	2.36	2.68	2.21	2.39	2.59	2.25	4.64	0.00
ThO_2	43.58	40.57	39.41	38.58	25.16	26.57	20.96	20.56	16.37	17.43	8.53	0.18
UO_2	3.17	2.84	2.30	2.63	6.15	6.09	4.61	4.54	4.95	6.41	3.38	0.07
SO_3	0.10	0.20	0.00	0.33	0.12	0.15	0.57	0.65	0.55	0.45	0.35	0.02
Cl	0.22	0.19	0.16	0.18	0.16	0.18	0.21	0.13	0.19	0.16	0.19	0.00
Total	97.31	99.24	93.90	97.85	95.52	96.46	96.82	95.58	96.69	95.69	95.72	98.38
Normalization based on Ca + REE + Th + U = 5000												
Si	2.579	2.402	2.465	2.394	2.700	2.763	2.061	2.108	2.147	2.091	2.257	0.037
P	0.186	0.372	0.219	0.458	0.126	0.112	0.619	0.573	0.628	0.672	0.504	2.864
Ca	3.294	3.341	3.357	3.386	2.854	2.787	3.335	3.317	3.223	3.299	2.785	4.971
La	0.110	0.150	0.140	0.150	0.390	0.390	0.310	0.320	0.380	0.340	0.580	0.010
Ce	0.150	0.200	0.180	0.200	0.590	0.580	0.480	0.480	0.600	0.520	0.910	0.010
Nd	0.020	0.040	0.040	0.040	0.110	0.130	0.090	0.100	0.110	0.100	0.200	0.000
Th	1.310	1.160	1.180	1.120	0.760	0.810	0.560	0.560	0.440	0.480	0.230	0.000
U	0.090	0.080	0.070	0.070	0.180	0.180	0.120	0.120	0.130	0.170	0.090	0.000
S	0.010	0.020	0.000	0.030	0.010	0.020	0.050	0.060	0.050	0.040	0.030	0.000
Cl	0.050	0.040	0.040	0.040	0.040	0.040	0.040	0.030	0.040	0.030	0.040	0.000

Melilite compositions vary continuously from almost pure akermanite to $akermanite_{55}gehlenite_{45}$. The $Mg/(Mg+Fe^{2+})$ ratio is generally high (0.96–0.98), but the most akermanite-rich compositions show more extensive $FeMg_{-1}$ exchange [$Mg/(Mg + Fe^{2+}) = 0.88–0.90$].

Phlogopite from the Flekkeren locality is characterized by $Mg/(Mg + Fe) > 0.9$ and considerable substitution toward the eastonite end-member (2.8–3.1 Al apfu when normalized to total cations − K = 14.00). F typically substitutes for about 10% of the OH.

Kalsilite commonly occurs intergrown with wollastonite. Spectacular graphic intergrowths of kalsilite and wollastonite with minor nepheline resemble textures formed by spinoidal decomposition (Fig. 2b). As these phases hardly can form by decomposition of a single pre-existing solid phase, we speculate that this texture results from rapid (metastable) reaction between the original potassium feldspar and calcite:

$$Kfs + Cc = Ks + Wo + CO_2 \quad (1)$$

Nepheline commonly occurs as irregular lamellae within kalsilite grains, but may also form separate grains that frequently are fringed by complex intergrowths of cancrinite and zeolite-group minerals (see below). Kalsilite contains very little Na whereas nepheline contains about 25 mol% kalsilite component.

The Flekkeren samples contain an extreme variety of garnets (see Table 3). Because of the presence of OH and Zr in many of these garnets, the structural formula has been calculated by assuming that Ca + Mg + Mn = 3.0. For the melanites, structural formulas have also been calculated by normalization to a total charge of 24, but the results are only marginally different. Three garnet types are classified as Stage I phases. Uvarovite ($X_{uv} \leq 0.9$) that predates or dates the peak assemblage nucleated on detritial chromite grains and is responsible for the strong green color of some hand specimens. Rare zirconian garnet (kimzeyite) was found in veinlets through the pre-Stage I uvarovite along with the Stage I Zr phase baghdadite (see below) and probably grew in a locally Zr-enriched system. Kimzeyite contains up to 18.4 wt% ZrO_2 (0.7 Zr pfu) and are low in Si because of the extensive $Zr^{6+}Al^{4+}Si^{4+}_{-1}Al^{6+}_{-1}$ substitution. Ti- and Cr-contents are high: 10–11 wt% TiO_2 and 1.7–2.4 wt% Cr_2O_3 (0.6–0.7 Ti and 0.1–0.15 Cr pfu). The dominating Stage I garnet grains are subhedral to anhedral melanite, occasionally with a core of uvarovite. The melanite compositions show good positive correlation between Mg, Ti, Cr, and Zr, reaching a maximum of approximately 9.4 wt% TiO_2, 5.7 wt% Cr_2O_3, and 2.0 wt% ZrO_2. A good negative correlation exists between the Mg and Si content of these garnets (Fig. 3), presumably reflecting increasing Ti^{4+}-content with increasing Ti-content. The uvarovite compositions plot on the Mg vs. Ti and Mg vs. Si trends defined by the melanite and Stage II grandite. Ignoring the uvarovites, there seems to be a gap in garnet composition in the range Mg = 0.06–0.1 apfu, separating Stage I melanites from Stage II grandite. Furthermore this gap reflects abrupt changes in the composition of zoned garnet with melanitic cores and granditic rims.

Cuspidine [$Ca_4Si_2O_7(F,OH)_2$] and baghdadite ($Ca_3ZrSi_2O_9$) are additional Ca phases that occur as small ($\approx$ 100 μm) grains in equilibrium with Cc+Wo+Mel (Fig. 4a). Baghdadite was originally described from a melilite skarn by Al-Hermezi et al. (1986). This occurrence of baghdadite is to our knowledge only the second reported. Baghdadite presumably formed by the breakdown of original detrital zircon through the reaction

$$Zrn + 2Cc + Wo = Bg + 2CO_2. \quad (2)$$

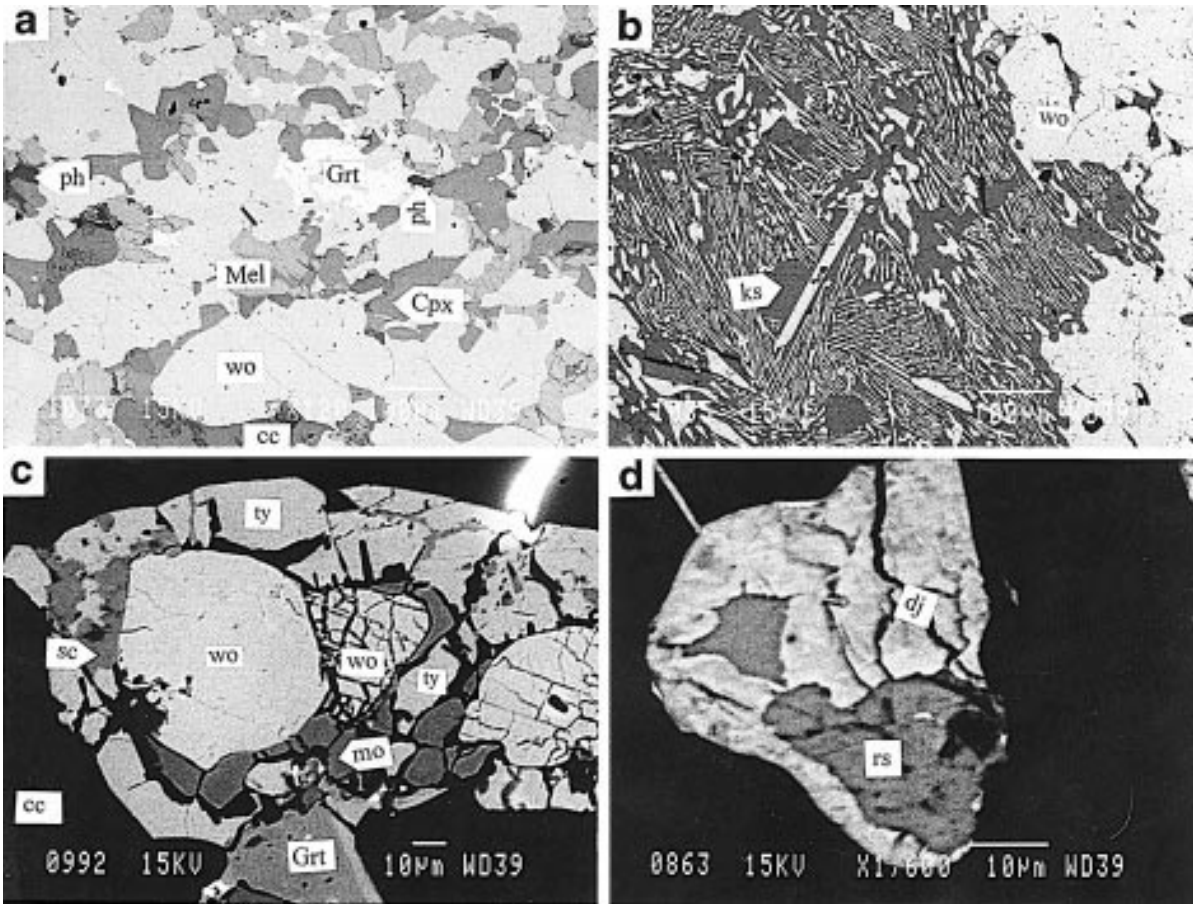

FIGURE 2. (**a**) Peak metamorphic assemblage composed of calcite, wollastonite, clinopyroxene (fassaite), phlogopite, melilite, and titanian garnet (melanite). Field of view 1 mm long. (**b**) BSE-image showing graphic intergrowth of wollastonite and kalsilite. Note variations in the orientation of the wollastonite lamellas along boundaries interpreted as original grain boundaries. (**c**) Formation of Stage II phases tilleyite, monticellite, and grandite garnet along original calcite-wollastonite grain boundaries. Also note the late growth of scawtite along fractures through the tilleyite and along the tilleyite-wollastonite boundary. (**d**) Rasvumite (core) and djerfisherite (rim) replacing an original pyrrhotite grain.

Baghdadite analyses show nearly perfect stoichiometric compatibility with the formula given by Al-Hermezi et al. (1986) (Table 3). In the Flekkeren samples about 15% of the Zr is substituted by Ti, giving the approximate formula $Ca_3Zr_{0.85}Ti_{0.15}Si_2O_9$. The cuspidine is close to the F end-member and contains variable Zr contents (0–1.7 wt% ZrO_2). The most Zr-rich samples coexist with baghdadite and may in fact reflect limited solid solution toward baghdadite, which also is a member of the wöhlerite-cuspidine group.

Calcite-free, calc-silicate layers have a Stage I assemblage composed of wollastonite, clinopyroxene, melanitic garnet or uvarovite, and potassium feldspar. An additional phase is scapolite, which has an ambiguous petrographic status in these rocks. It sometimes occurs as millimeter-sized poikiloblasts with inclusions of the peak assemblage minerals and in many cases clearly replaces potassium feldspar. Scapolite growth is associated with alkali-exchange and introduction of Cl to the metasedimentary rocks. Accessory minerals include zircon, pentlandite, pyrrhotite, löllingite, chromite, scheelite, galena, sphalerite, uraninite, a LREE-silicate (possibly stillwellite), an unidentified oxide of Ca, LREE, Th, U, Ti, and Nb and Si-rich apatite group minerals. Zircon is recrystallized and remobilized during the high-grade metamorphism and occurs as euhedral porphyroblasts or as irregular masses along the silicate grain-boundaries.

Various Th and LREE-enriched silicate apatites formed at the expense of original apatite in layers enriched in heavy accessory minerals during contact metamorphism. These can occasionally be observed as coronas around the original apatite grains (Fig. 4b). Brownish, Th-rich, varieties (X1 in Table 1) are commonly associated with thorite. Thorianite is observed as a reaction product when the original silicate apatites break down during hydration of metamict grains to an amorphous substance with apatite-like composition. Silicate phosphate analyses are listed in Table 4. The composition space of the silicate

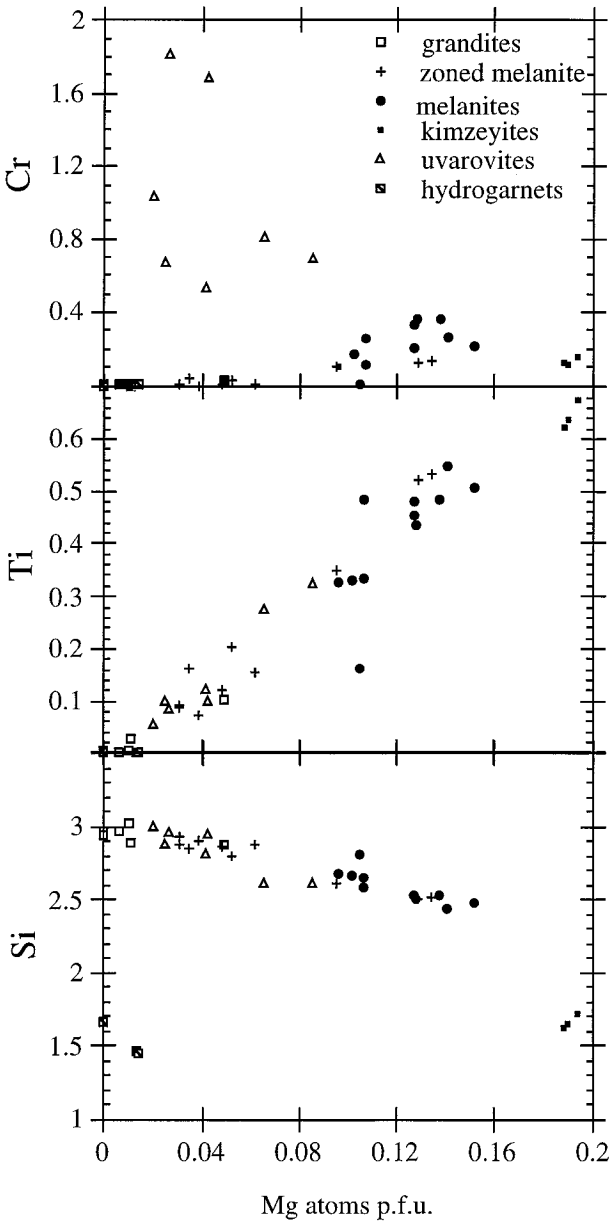

FIGURE 3. Cr, Ti, and Si apfu vs. Mg atoms for the various types of garnet observed in the Flekkeren samples. Crosses (zoned melanite) refer to data from a single-zoned garnet grain.

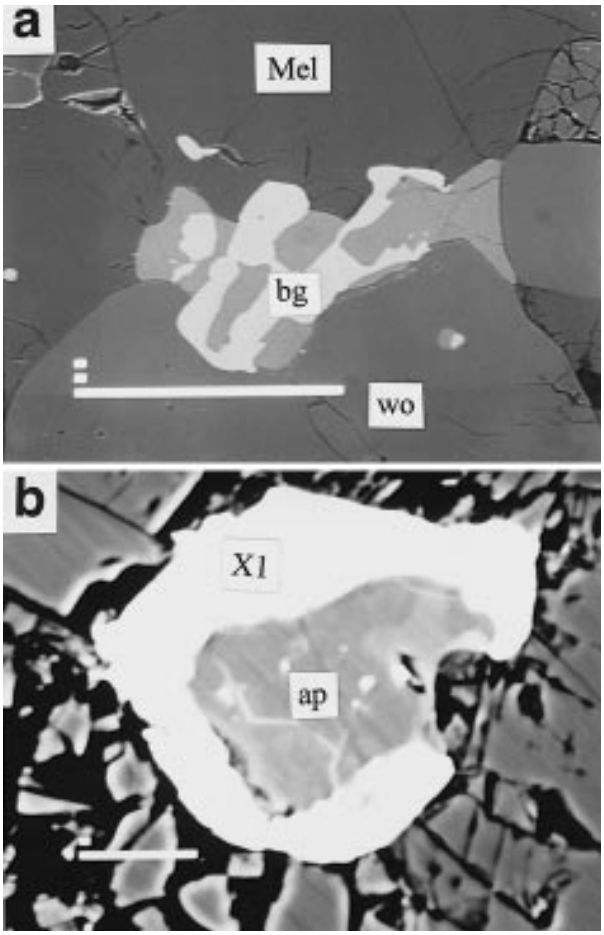

FIGURE 4. BSE-images showing (**a**) Coexistence of baghdadite and the related mineral cuspidine in a matrix of melilite and wollastonite. This system is calcite saturated. Scale bar is 100 μm. (**b**) Th-rich silicate apatite (X1) forming as a corona around an original apatite grain. Scale bar 10 μm.

apatites can be largely described by the end-members apatite [$Ca_5P_3O_{12}(OH)$], britholite [$LREE_3Ca_2Si_3O_{12}(OH)$], and the new species X1 [$Ca_{3.5}(Th,U)_{1.5}Si_3O_{12}(OH)$]. Minor substitutions occur along the vectors $Cl(OH)_{-1}$ (0.035 ± 0.005 Cl pfu) and $SiSP_{-2}$ (0.035 ± 0.015 S pfu). Silicate phosphate analyses have been normalized assuming that Ca+Th+U+La+Ce+2Nd = 5.000. Doubling of the Nd content was done to account for the presence of REE heavier than Nd and is based on the relative concentrations of the three analyzed LREE assuming a log-linear REE-cation size vs. concentration pattern. Errors introduced by doing this are small in these extremely LREE-enriched apatites. Normalization including the tetrahedral coordinated cations is not possible as these silicate apatites may contain significant amounts of CO_3 and B, which are not measured by the EMP. The analyzed samples range in composition from $ap_{17}X1_{21}br_{62}$ to $ap_6X1_{85}br_9$, but cluster around $ap_{20}X1_{40\text{-}45}br_{40\text{-}35}$ (Fig. 5). The U content is constant (4.5 ± 1.5 wt% UO_2) and does not vary systematically with Th content but is low (2.3–3.2 wt% UO_2) in the most Th-rich samples (>1.0 Th pfu). The limited variations in the apatite content of the analyzed samples indicate that the main substitution mechanism is $ThCaLREE_{-2}$. However, a positive correlation exists between the Th + U content and the Si deficiency (defined as Th + 2LREE − Si) in the tetrahedral position, which may be explained by moderate coupled Th + B substitution for Ca and P or LREE and P [e.g., along the vector $ThB(CaP)_{-1}$] (Burt 1989). The total sum of the EMP analyses is low for Th-poor samples (Table 3). This

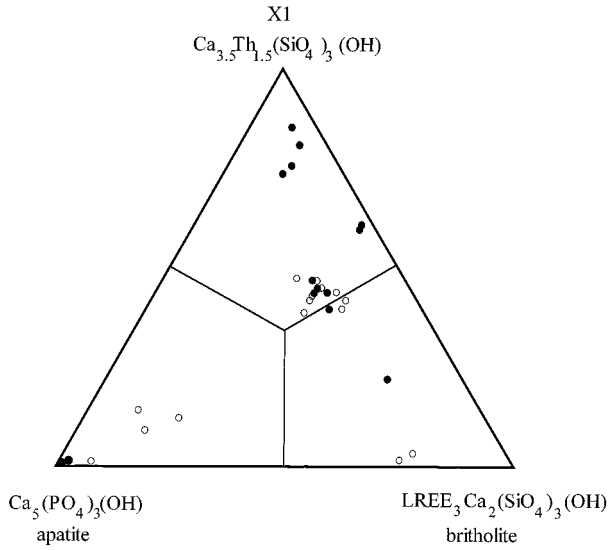

FIGURE 5. Compositional variations among apatites and silicate apatites showing that most analyses plot within the field of the new end-member species X1. Open symbols show the composition of grains that give low totals in the electron microprobe analyses. This is probably partly due to hydration of metamict grains and partly due to a significant concentration of B and or C.

is probably due to a significant H_2O content, possibly resulting from hydration of metamict grains.

Stage II

The transition from Stage I to Stage II assemblages in calcite-saturated layers is marked by the occurrence of monticellite, tilleyite, vesuvianite, grandite garnet (poor in Ti and Cr, see Table 3), Al-poor diopside, and occasional hillebrandite. Retrogression defining the onset of Stage II occurs pervasively through the Stage I assemblages. Tilleyite forms as a corona between calcite and wollastonite (Fig. 2c) and is in textural equilibrium with monticellite probably forming at the expense of melilite. Tilleyite and monticellite may form through the reactions:

$$2Wo + 3Cc = Ty + CO_2 \quad (3)$$

$$3Cc + 2Ak = Ty + 2Mo + CO_2 \quad (4)$$

Monticellite also coexists with garnet and vesuvianite and is observed in reaction rims around melilite with wollastonite and calcite. In this case it may form by the fluid-absent reaction:

$$Ak = Wo + Mo \quad (5)$$

Monticellite falls into two compositional groups, one with Mg/(Mg + Fe) = 0.67 − 0.77 and one coexisting with tilleyite and with Mg/(Mg + Fe) > 0.95.

Vesuvianite occasionally forms euhedral porphyroblasts with inclusions of wollastonite and melilite or occurs as millimeter-thick layers alternating with granditic garnet layers. The Mg/(Mg + Fe) ratios for four samples are within the range 0.7–0.8 (all Fe assumed divalent).

Grossular-rich Stage II garnet ($X_{gr} > 0.6$), typically is observed as rims on Stage I melanites or as alteration rims between other Stage I minerals but sometimes as euhedral poikiloblasts with numerous calcite and wollastonite inclusions. On the basis of the textural observations the most likely candidates for reactions responsible for vesuvianite and garnet formation are:

$$3Wo + 2Ak + 2Ge + CO_2 + 2H_2O = vs + Cc \quad (6)$$

$$2Wo + Ge + CO_2 = Gr + Cc \quad (7)$$

Both these reactions include breakdown of the gehlenite (ge = $Ca_2Al_2SiO_7$) component of the Stage I melilites. Al-poor diopside formed as a rim or neoblast around peak-metamorphic augitic pyroxene (fassaite) and is commonly associated with grandite garnet. The formation of these phases may be described by the breakdown of the calcium-tschermaks (cats) component of the pyroxene through the continuous equilibrium:

$$Cats + Wo = Gr \quad (8)$$

The Stage I pyrrhotite is frequently surrounded by a corona of rasvumite, which again may be replaced by djerfisherite (Fig. 2d). The formation of these sulfides is spatially associated with formation of other Stage II minerals. Djerfisherite may also replace pyrrhotite without any intervening stage of rasvumite growth. Rasvumite and djerfisherite are rare potassium iron sulfides previously reported from alkaline intrusions (e.g., Czamanske et al. 1979) and from enstatite chondrites (Heide and Wlotzka 1995). These phases are interpreted to have formed by reactions such as (stoichiometry dependent on the pyrrhotite composition):

$$Wo + 2Cc + 2Ks + 6Pyh = 2Rs + Gr + 2CO_2 \quad (9)$$

$$3Wo + 6Cc + 6Ks + 25Pyh = Dj + 3Gr + 6CO_2 \quad (10)$$

or by the addition of K from externally derived fluids. Rasvumite is nearly stoichiometric KFe_2S_3. Djerfisherite has been described as $K_6Cu(Fe,Ni)_{12}S_{14}$, as $K_6Na(Fe,Ni)_{24}S_{26}Cl$, and as $K_6(Fe,Ni)_{25}S_{26}Cl$ (cf. Czamanske et al. 1979). The analyzed samples fall into two populations, one Cl-bearing and one essentially Cl-free. Ni was only analyzed in the Cl-poor samples, which contain 4–5 Ni apfu. Furthermore the X-ray spectrum indicated significant amounts of Co and Cu.

Stage III

Examining the samples from Flekkeren using UV light has revealed diffuse veinlets that contain highly fluorescent sodalite in a symplectite (grain size 10–50 μm) containing kalsilite, potassium felspar, and calcite (Fig. 6a). Wollastonite, clinopyroxene, and titanite occur in this symplectitic matrix. These assemblages are referred to as Stage III assemblages below. Clinopyroxene grains in these veinlets are extensively zoned and show sharp compositional changes from a green acmite rich core (0.17–0.18 Na pfu), to an intermediate zone (0.071–0.076 Na

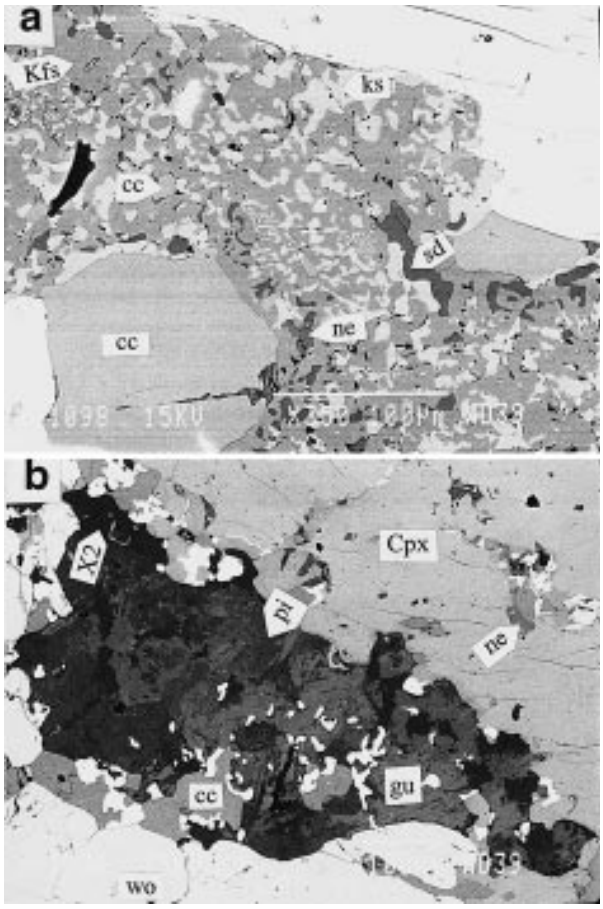

FIGURE 6. BSE-images showing (**a**) Symplectite composed of the Stage III phases kalsilite, K-feldspar, sodalite, nepheline, and calcite between larger wollastonite and calcite grains. Scale bar is 100 μm. (**b**) Complex intergrowths of guiseppettite, phillipsite, thomsonite, calcite, and an unknown zeolite-like mineral (X2) replacing an original nepheline grain. Nepheline can still be found as inclusions in the fassaitic clinopyroxene porphyroblast in the upper right corner of the BSE-image. Field of view about 0.7 mm long.

pfu) to a colorless rim (0.048–0.056 Na pfu), which is in optical discontinuity with the core.

Stage IV

Stage IV includes minerals occurring as late products of retrogressive reactions affecting Stage I–III minerals and in most cases their occurrence is confined to local subdomains in the samples. Many of these minerals are very fine grained and care was taken to avoid intergrowths and poorly defined grains during electron microprobe analysis. All phases described below show uniform extinction in cross-polarized light and are homogenous at the 1 μm scale. Microprobe analyses of different grains have given consistent results.

Alteration products after matrix nepheline grains are complexly intergrown (Fig. 6b) and include several phases including the sulfate-bearing cancrinite-group mineral giuseppettite [representative formula: $K_{2.5}Na_{4.5}Ca_{0.9}Al_6Si_6O_{24}(SO_4)_{1.3}Cl_{0.3}$] and the zeolites thomsonite (nearly ideal end-member composition) and phillipsite (representative formula: $KNa_{0.1}Ca_{1.1}Al_{3.3}Si_{4.7}O_{16}{\cdot}6H_2O$). An additional, and to our knowledge not yet described, zeolite-like mineral with the approximate formula $Na_{2.3}Ca_{0.8}Al_4Si_4O_{16} \cdot X\ H_2O$ (X2 in Table 1) is also present. Low-grade tectosilicates formed along with calcite during wollastonite consumption. Scawtite occurs as fringes along grain boundaries and fractures through tilleyite (Fig. 2c).

Stage IV hydrogrossular is invariably Al-rich (>1.8 Al pfu) and occurs along grain boundaries or fractures through Stage II grandite garnet. It contains 1.45–1.7 Si pfu, (5.2–6.2 OH-groups pfu) and are classified as hibschites and katoites (cf. Passaglia and Rinaldi 1984).

Fractures through large wollastonite grains (100 μm to 1 mm long) in the Stage III veinlets invariably contain a colorless unidentified phase (X3 in Table 1) that may represent a new mineral species. The formula inferred from electron microprobe analyses is $[Na_2Ca_4Si_6O_{15}(OH)_4]$. Another unknown Ca,Si-rich mineral species (X4 in Table 1) was found as fracture fillings through clinopyroxene grains along with mineral X3. Tobermorite and smectite (saponite) represent the latest and very fine-grained alteration products from calc-silicates observed in these samples, and opal was identified as a coating on late fractures.

PETROLOGY

In the following, we attempt to determine the varying temperature and fluid composition conditions during the metamorphic history of these rocks through an analysis of heterogeneous phase equilibria. As the activity-composition relations for Ti-rich garnets and vesuvianite solid-solutions are essentially unknown, the Flekkeren assemblages were analyzed within the composition space $KAlO_2$-CaO-MgO-SiO_2-H_2O-CO_2. Pressure estimates on the basis of stratigraphic reconstructions (Vogt 1907; Dahlgren, unpublished results) and fluid inclusion work (Olsen and Griffin 1984; Andersen 1990) are in the range 700–1000 bar. Figure 7 and 8 show isobaric T-X_{CO2} and T-X(O) diagrams for this end-member system calculated at 1000 bar, applying the VERTEX program of Connolly (1990) and a revised version of the thermodynamic database of Holland and Powell (1990). For binary H_2O-CO_2 fluids, the CORK equation of state (Holland and Powell 1991) was used. For graphite saturated assemblages, we applied the GCOH and GCOHS equations of state of Connolly and Cesare (1993).

As the petrographic status of the observed graphite in these rocks is uncertain, phase diagrams were calculated by assuming binary H_2O-CO_2 fluids or assuming graphite saturation. The observed Stage I mineral assemblage Cc-Wo-Ph-Cpx-Ak-Ks-fluid (Table 2) corresponds to equilibration near the isobaric Invariant Point 8 in Figure 7a, located at $T \approx 870$ °C, $X_{CO_2} \approx 0.38$. The diopside-absent reaction is stable on the low temperature side of Invariant Point 8, and thus there is a net production of pyroxene in this point (cf. Carmichael 1991). This is con-

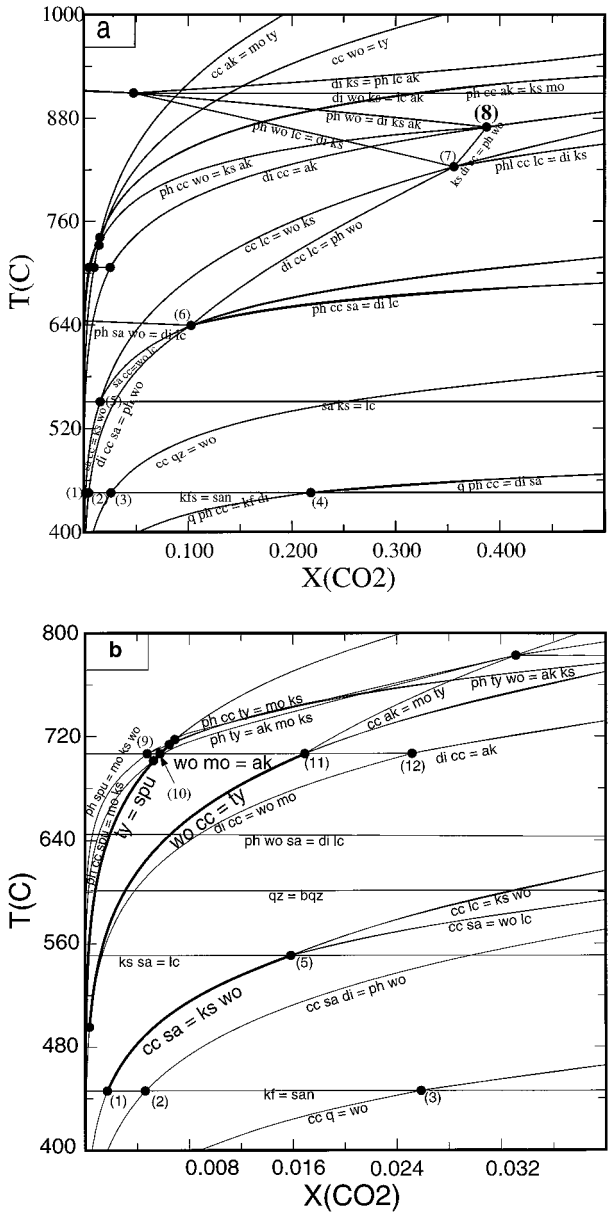

FIGURE 7. Simplified T-X_{CO_2} diagrams calculated at P = 1000 bar for the pure $KAlO_2$-CaO-MgO-SiO_2-H_2O-CO_2 system excluding equilibria that are irrelevant with the present variability in bulk composition (i.e., equilibria involving forsterite, Ca-poor pyroxene, and amphibole). Reactions are always written with the high-temperature assemblage to the right of the equality sign. (**a**) T-X_{CO_2} diagram for the region relevant to the Stage I assemblage. (**b**) T-X_{CO_2} diagram showing in more detail equilibria relevant for the retrograde Stage II and III assemblage. The regions of possible stability of these assemblages are limited by the reactions shown by bold lines. Abbreviations not included in Table 1: Sa = sanidine; Lc = leucite; Q = quartz, Bq = beta quartz; Spu = spurrite.

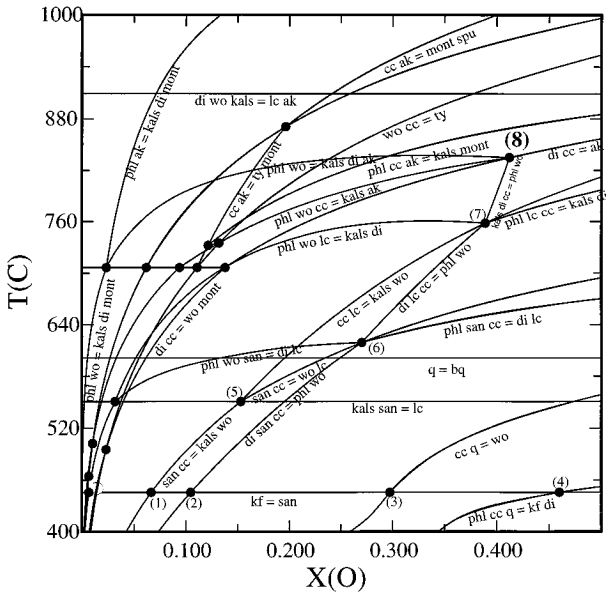

FIGURE 8. T-X(O) projections calculated at P = 1000 bar for the pure $KAlO_2$-CaO-MgO-SiO_2-C-O-H system with graphite saturation.

sistent with the observed poikiloblastic texture of the pyroxene in these rocks. Uncertainties in the position of Invariant Point 8 mainly stems from possible errors in the activity corrections of the phase components Di, Ak, and Ph. The univariant reactions intersect at acute angles and thus minor errors in the relevant activities give large effects on the calculated X_{CO_2}-value. Test experiments with several activity models and with varying compositions of the phases involved suggest a maximum range for T of 820–870 °C and X_{CO_2} of 0.2–0.4. Lowering the pressure to 700 bar gives a reduction in T by about 25 °C and an increase in X_{CO_2} by 0.03 units for the end-member system. The inferred peak temperature is slightly higher than the inferred solidus (approximately 800 °C) for a compositionally similar monzonite intrusion in the Sande Cauldron further north in the Oslo Rift (Andersen 1984).

The stability of the retrograde assemblage Ty-Mo-Wo-Cc, can be inferred from Figure 7b. Wollastonite + monticellite puts an upper limit on the metamorphic temperature of about 710 °C, and the presence of tilleyite at such temperatures requires that $X_{CO_2} \leq 0.016$. Coexistence of monticellite and kalsilite restricts the stability of the Stage II assemblage to a region near Invariant Point 10 at $T \approx$ 710 °C, $X_{CO_2} \approx 0.005$. Hence, these diagrams suggest a change from 20–40% CO_2 in the metamorphic fluid during peak metamorphic conditions to almost C-free fluids during formation of the Stage II assemblage.

The Stage III assemblage Ks-Kfs-Wo-Cc constrain the maximum temperature to about 550 °C and the composition of a binary H_2O-CO_2 fluid to $X_{CO_2} < 0.016$ (Fig. 7b).

At graphite saturation, the assumption of a binary H_2O-CO_2 fluid is incorrect. Figure 8 shows a T-X(O) diagram constructed for the end-member system at 1000 bars. A

projection of COH-fluid compositions through graphite leads to a binary representation of the fluid in the H-O system where $X(O)$ [= O/(O + H)] varies from 0 to 1 as the fluid composition changes from the C-H join to the C-O join and is ⅓ for pure H_2O (Connolly 1995). $X(O)$ is proportional to the oxygen fugacity in GCOH fluids. The estimates of the peak metamorphic temperature (near Invariant Point 8) is not sensitive to the absence or presence of graphite. In the T-$X(O)$ diagram Invariant Point 8 is located at $T \approx 840$ °C, $X(O) \approx 0.4$. However, the fluid composition corresponding to this $X(O)$ value deviates significantly from a binary H_2O-CO_2 fluid and contains about 14 mol% CH_4. Adding S as a fluid component and buffering the fluid composition by pyrrhotite with a Fe/S ratio of 0.93 (the most Fe-rich pyrrhotite measured in the Flekkeren samples), the resulting fluid composition is 40% H_2O, 30% CO_2, 10% H_2S, 10% CH_4, 5% CO, and 5% H_2.

Phase relations, calculated including Al_2O_3 as an additional thermodynamic component, are consistent with the formation of garnet and vesuvianite by Reactions 6 and 7 at temperatures below peak temperature. However, the exact positions of these equilibria are associated with considerable uncertainty because of uncertainties in thermodynamic data and solid solution models for vesuvianite and melanitic garnets.

Several solid-solid continuous equilibria can be written among the possible phase components to constrain metamorphic temperatures from fluid-independent reactions, but none have proved useful because of small entropy changes and correspondingly great sensitivity to activity-concentration models and uncertainties in available thermodynamic data. However, several useful observations can be made from variations in the mineral composition. The extensive Al substitution in the pyroxene reflects the high temperature of metamorphism and is buffered by Reaction 8, which is characterized by a positive change in both entropy and volume. This equilibrium is probably one of the most useful continuous reactions in recording relative temperature variations within and among contact aureoles in calcareous rocks where the fluid composition may be variable. Likewise, the Mg content of the garnet is likely to correlate positively with the metamorphic temperature because almost every Fe-Mg exchange equilibrium between garnet and other ferromagnesian minerals produces relative Fe enrichment in the garnet. As the Al content in pyroxene and Mg content in garnet correlate positively with the temperature of equilibration, the Ti contents of both pyroxene and garnet also correlate positively with temperature. Cr shows the same behavior as Ti, but the Cr content of the garnet is strongly affected by local Cr sources in its environment and thus shows much more scatter than does the Ti-content.

Discussion

The mineral assemblages from the Flekkeren locality are unusual for metamorphic rocks, mainly because rocks of such bulk composition rarely experience such high temperatures in combination with low pressures. Many of the observed phases are indeed more common in some Si-poor alkaline intrusions such as ijolite-series rocks and ultramafic lamprophyres (e.g., Sørensen 1979; Dahlgren 1987).

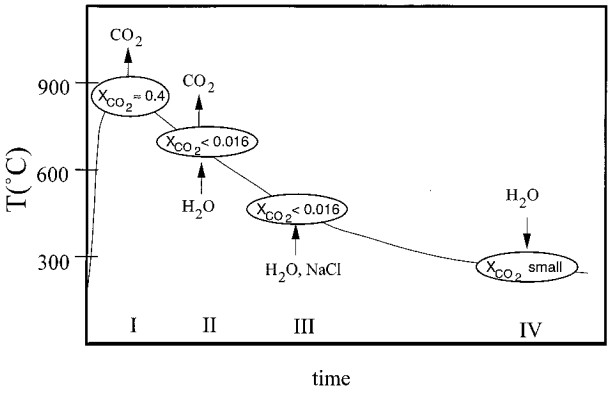

Figure 9. Schematic temperature-time evolution for the Flekkeren megaxenolith superimposed on a T-t curve believed to have a shape typical for regions near the top of a cooling intrusive. Heating during the prograde stage lead to devolatilization reactions causing a relatively high C content in the pore fluids at Stage I. This was followed by an infiltration controlled increase in the H_2O content through influx of magmatic (upward directed arrows) and later of meteoric fluids (downward directed arrows) during Stage IV.

The large number of minerals present in these rocks is clearly related to metamorphic reactions taking place throughout the metamorphic history, and these reactions are partly driven by the interactions with externally derived magmatic and meteoric fluids. The metamorphic history inferred from the petrology is schematically illustrated in Figure 9 and is superimposed on a T-t curve that is believed to be typical for regions near the top of a cooling intrusion (cf. Hanson 1995; Fig. 8). We believe that the petrologic analysis gives a reasonably reliable indication of the conditions of formation for the observed Stage I mineral assemblage, indicating a relatively CO_2-rich (or at least C-rich) pore fluid during peak metamorphism. However, in the present geological setting, where a megaxenolith of impure limestone fell into a partly molten intrusion, we cannot expect the rapidly heating metasedimentary rock to follow a progressive reaction path predicted from an equilibrium phase diagram. The observed graphic intergrowths between kalsilite and wollastonite (Fig. 2b) reflect short transport distances during the reaction and are more readily explained by rapid non-progressive metamorphic breakdown of original potassium feldspar and calcite than by progressive reactions along a buffered T-X_{CO_2} path that would have lead to the production of leucite as an intermediate but non-observed species.

During rapid heating of a calcareous rock embedded in a partly crystallized intrusion, the fluid pressure within the xenolith rapidly rose through devolatilization reac-

tions to reach or even exceed the fluid pressure in the surrounding intrusive. This hindered major fluid infiltration into the xenolith in agreement with available O isotope results obtained from the carbonates. At this stage (Stage I) the fluid composition in the xenolith was either buffered by decarbonation reactions or, in the non-equilibrium case, controlled by the stochiometry of the ongoing reactions. This caused a rise in the CO_2 content (and CH_4 content at reducing conditions) of the metamorphic fluids toward peak temperature conditions. When cooling started, the total solid volume of the xenolith was considerably reduced because of volatile loss (occasionally exceeding 10% of the initial volume, depending on the initial carbonate-silicate ratio). Unless this volume loss was accommodated by compaction, which may have been a relatively slow process at the time-scales of the heating of these contact metamorphic rocks, the reduction in total solid volume made the xenolith more permeable and susceptible to pervasive influx of external fluids. Thus, the progressive stage of metamorphism leading to the Stage I assemblage is strikingly similar to the industrial production of highly porous cement clinker by rapid heating at low P of a clay-limestone mixture, with a bulk composition similar to some of the Flekkeren samples.

This model explains why the post-peak (Stage II–IV) assemblage reflects C-poor, H_2O-dominated magmatic or meteoric fluids. The pervasive formation of the Stage II assemblage is in many respects in contrast to the more common situation during retrogressive metamorphism where volatilization reactions usually depend on fluid access around fractures, faults, or other highly permeable zones generated after the formation of the peak assemblage.

However, Stage III retrogression is associated with veins or veinlets. This is consistent with retrogression at lower temperature where thermal contraction may have led to fracturing and more localized access of magmatic and possibly meteoric fluids to generate veins in the metasedimentary rocks. The growth of sodalite during Stage III implies an addition of Cl to the system. Influx of brines through brittle fractures is a common feature in contact aureoles in the Oslo rift during cooling from peak metamorphic conditions and is ascribed to the late release of saline magmatic liquids that were relatively immobile during peak metamorphism because of the low permeability of the country rocks at this stage (Jamtveit and Andersen 1993).

Stage IV marks the onset of the growth of very fine grained low-temperature phases such as zeolites. At this stage the magmatic system was completely crystallized and the most likely source for externally derived fluid is meteoric water.

Acknowledgments

Discussions and assistance from Odd Nilsen and Henrik Svensen at the Department of Geology, University of Oslo, and the supporting engagement of Alf Olav Larsen at Norsk Hydro, Research Centre, Porsgrunn, are greatly acknowledged. Very thorough reviews by an anonymous referee and by Tom Hoisch significantly improved this paper. This work was supported by grant no. 110578/410 from the Norwegian Research Council.

References cited

Al-Hermezi, H.M., McKie, D., and Hall, A.J. (1986) Baghdadite, a new calcium zirconium silicate mineral from Iraq. Mineralogical Magazine, 50, 119–123.

Andersen, T. (1984) Crystallization history of a Permian composite monzonite-alkali syenite pluton in the Sande Cauldron, Oslo rift, S. Norway. Lithos 17, 153–170.

——— (1990) Melt-mineral-fluid interaction in peralkaline silicic intrusions in the Oslo Rift, Southeast Norway IV: Fluid inclusions in the Sande nordmarkite. Norges Geologiske Undersøkelser Bulletin, 317, 41–54.

Bjørlykke, K. (1974) Depositional history and geochemical composition of Lower Palaeozoic epicontinental sediments from the Oslo Region. Norges Geologiske Undersøkelse Bulletin, 305, 1–81.

Burt, D.M. (1989) Compositional and phase relations among rare earth element minerals. In Mineralogical Society of America Reviews in Mineralogy, 21, 259–307.

Carmichael, D.M. (1991) Univariant mixed-volatile reactions: Pressure-temperature phase diagrams and reaction isograds. Canadian Mineralogist, 29, 741–754.

Connolly, J.A.D. (1990) Multivariable phase diagrams: an algorithm based on generalized thermodynamics. American Journal of Science, 290, 666–718.

——— (1995) Phase diagram methods for graphitic rocks and application to the system C-O-H-FeO-TiO2-SiO2. Contributions to Mineralogy and Petrology, 119, 94–116.

Connolly, J.A.D. and Cesare, B. (1993) C-O-H-S fluid composition and oxygen fugacity in graphitic metapelites. Journal of metamorphic geology, 11, 379–388.

Czamanske, G.K., Erd, R.C., Sokolova, M.N., Dobrovol'skaya, M.G., and Dmitrieva, M.T. (1979) New data on rasvumite and djerfisherite. American Mineralogist, 64, 776–778.

Dahlgren, S. (1987) The satellitic intrusions in the Fen carbonatite-alkaline rock province, Telemark, Southeastern Norway. Ph.D. thesis, 350 p. University of Oslo.

——— (1998) Map sheet 1713 IV Nordagutu, bedrock geology. Scale 1: 50000. Geological Survey of Norway, in press.

Goldschmidt, V.M. (1911) Die Kontaktmetamorphose im Kristianiagebiet. Vitenskaps-selskapets Skrifter. I., Matematisk Naturvitenskapelig Klasse, No. 1, 483 p.

Hanson, R.B. (1995) The hydrodynamics of contact metamorphism. Geological Society of America Bulletin, 107, 595–611.

Heide, F. and Wlotzka, F. (1995) Meteorites, 231 p. Springer-Verlag, Heidelberg.

Holland, T.J.B. and Powell, R. (1990) An enlarged and updated internally consistent dataset with uncertainties and correlations: the system K_2O-Na_2O-Cao-MgO-FeO-Fe_2O_3-Al_2O_3-TiO_2-SiO_2-C-H_2-O_2. Journal of Metamorphic Geology, 8, 89–124.

——— (1991) A compensated-Redlich-Kwong (CORK) equation of state for volumes and fugacities of CO_2 and H_2O in the range 1 bar to 50 kbar and 100–1600 C. Contributions to Mineralogy and Petrology, 109, 265–273.

Inderst, B. (1987) Mischkristalle und fluide phase (H_2O-CO_2) bei hochtemperature dekarbonatisierungsreaktionen in zwei thermalaureolen. PhD thesis, 215 p. Ludwig-Maximillans-University, München.

Jamtveit, B. and Andersen, T. (1993) Contact metamorphism of layered shale-carbonate sequences in the Oslo rift: III. The nature of skarn-forming fluids. Economic Geology, 88, 830–849.

Jamtveit, B., Bucher-Nurminen, K., and Stijfhoorn, D.E. (1992a) Contact metamorphism of layered shale-carbonate sequences in the Oslo rift: I. Buffering,infiltration and the mechanisms of mass transport. Journal of Petrology, 33, 377–422.

Jamtveit, B., Grorud, H.F., and Bucher-Nurminen, K. (1992b) Contact metamorphism of layered shale-carbonate sequences in the Oslo rift: II. Migration of isotopic and reaction fronts around cooling plutons. Earth and Planetary Science Letters, 114, 131–148.

Jamtveit, B., Grorud, H.F., and Ragnarsdottir, K.V. (1997) Flow and transport during contact metamorphism and hydrothermal activity: Examples

from the Oslo rift. In B. Jamtveit and B.W.D. Yardley, Eds., Fluid flow and transport in rocks: Mechanisms and effects, p. 57–82. Chapman and Hall, London.

Joesten, R. (1983) Grain growth and grain-boundary diffusion in quartz from the Christmas Mountains (Texas) contact aureole. American Journal of Science, 238-A (Orville Volume), 233–254.

Olsen, K.I. and Griffin, W.L. (1984) Fluid inclusion studies of the Drammen granite, Oslo Paleorift, Norway: I. Microthermometry. Contributions to Mineralogy and Petrology, 87, 1–14.

Passaglia, E. and Rinaldi, R. (1984) Katoite, a new member of the $Ca_3Al_2(SiO_4)_3$-$Ca_3Al_2(OH)_{12}$ series and a new nomenclature for the hydrogrossular group of minerals. Bulletin Mineralogy, 107, 605–618.

Pedersen, L.E., Heaman, L.M., and Holm, P.M. (1995) Further constraints on the temporal evolution of the Oslo Rift from precise U-Pb zircon dating in the Siljan-Skrim area. Lithos, 34, 301–315.

Sørensen, H., Ed. (1979) The alkaline rocks, 622 p. Wiley, New York.

Sundvoll, B., Neumann, E.R., Larsen, B.T., and Tuen, E. (1990) Age relations among Oslo Rift magmatic rocks: implications for tectonic and magmatic modelling. Tectonophysics, 178, 67–87.

Svensen, H. (1996) A phase petrological analysis of contact metamorphic lower palaeozoic sedimentary rocks from the Oslo graben, Norway. Ph.D. thesis, 136 p. University of Oslo.

Svensen, H. and Jamtveit, B. (1998) Contact metamorphism of shales and carbonates from the Grua area, the Oslo rift, Norway: A phase petrological study. Norsk Geologisk Tidsskrift, in press.

Tracy, R.J. and Frost, B.R. (1991) Phase equilibria and thermobarometry of calcareous, ultramafic and mafic rocks, and iron formations. In Mineralogical Society of America Reviews in Mineralogy, 26, 207–289.

Vogt, J.H.L. (1907) Über die Erzgange zu Traag in Bamble, Norwegen. Zeitschrift zur Praktische Geologie, 15, 210–216.

Williams-Jones, A.E. (1981) Thermal metamorphism of siliceous limestone in the aureole of Mount Royal, Quebec. American Journal of Science, 281, 673–696.

Manuscript received November 20, 1996
Manuscript accepted July 23, 1997